

1 **Decadal Changes of Connections among late-spring Snow cover in West**  
2 **Siberia, summer Eurasia Teleconnection and O<sub>3</sub>-related meteorology in**  
3 **North China**

4 Zhicong Yin<sup>123</sup>, Yu Wan<sup>1</sup>, Huijun Wang<sup>123</sup>

5 <sup>1</sup>Key Laboratory of Meteorological Disaster, Ministry of Education / Joint International Research Laboratory of  
6 Climate and Environment Change (ILCEC) / Collaborative Innovation Center on Forecast and Evaluation of  
7 Meteorological Disasters (CIC-FEMD), Nanjing University of Information Science & Technology, Nanjing  
8 210044, China

9 <sup>2</sup>Southern Marine Science and Engineering Guangdong Laboratory (Zhuhai), Zhuhai, China

10 <sup>3</sup>Nansen-Zhu International Research Centre, Institute of Atmospheric Physics, Chinese Academy of Sciences,  
11 Beijing, China

12 **Corresponding author:** Zhicong Yin (yinzhc@nuist.edu.cn)

13 **Address:** No. 219 Ningliu Road, Pukou District, Nanjing University of Information Science & Technology,  
14 Nanjing 210044, China

15 **Tel.:** (+86) 136 5516 1661

16

17

18

19 **Abstract.** Severe surface ozone (O<sub>3</sub>) pollution frequently occurred in North China and obviously damages human  
20 health and ecosystems. The meteorological conditions effectively modulate the variations in O<sub>3</sub> pollution. In this  
21 study, the interannual relationship between O<sub>3</sub>-related meteorology and late-spring snow cover in West Siberia  
22 was explored, and the reasons of its decadal change were also physically explained. Before mid-1990s, less snow  
23 cover could enhance net heat flux and stimulate positive phase of the Eurasia (EU) teleconnection in summer. The  
24 positive EU pattern resulted in hot-dry air and intense solar radiation in North China, which could enhance the  
25 natural emissions of O<sub>3</sub> precursors and photochemical reactions in the atmosphere closely related to high O<sub>3</sub>  
26 concentrations. However, after the mid-1990s, the south edge of the dense snow cover area in West Siberia shifted  
27 northward by approximately 2° in latitude and accompanied radiation and heat flux also retreated toward the polar  
28 region. The connections among snow anomalies, EU pattern and surface O<sub>3</sub> became insignificant and thus  
29 influenced the stability of the predictability.

30 **Key words:** Eurasia pattern; ozone pollution; snow cover; sea ice; Arctic

## 31 1. Introduction

32 The Eurasia teleconnection (EU) pattern is a major quasistationary wave train in the Northern Hemisphere  
33 (Wallace and Gutzler, 1981; Wang and Zhang, 2015) and effectively linked the climate variability between the  
34 polar region and eastern China (Wang and He, 2015). The EU pattern appears in all seasons and consists of centers  
35 of geopotential height anomalies over polar region, Mongolia and North China, and the Yellow Sea and Japan Sea  
36 (Liu et al., 2014). The impacts of the EU pattern on the Eurasian climate have been investigated by many previous  
37 studies. The phase and intensity of the EU pattern have important impacts on the East Asia winter monsoon (Lim  
38 and Kam, 2016), as well as on the Siberian High (Gong et al., 2001), subtropical jet and East Asian trough (Liu  
39 and Chen, 2012). The enhanced winter monsoons resulted in lower temperatures and less precipitation in East  
40 China (Yan et al., 2003). Likewise, the EU pattern significantly influenced the dispersion conditions in North  
41 China and thus played important roles in local haze pollution (Li et al., 2019). In summer (June-July-August, JJA),  
42 the EU pattern influenced the Ural-blocking high and the East Asian trough and thus played important roles in the  
43 variability of summer precipitation over China (Zhang et al., 2018). Similarly, severe summer droughts in North  
44 China also had close relationships with the largest anomalies of the EU pattern (Wei et al., 2004). For example,  
45 the EU-like anomalous atmospheric circulations in summer 2014 resulted in an above-normal East Asian trough  
46 and a southward shift of the west Pacific subtropical high. Consequently, North China suffered from its most  
47 severe drought during the period of 1979–2014 (Wang and He, 2015). Moreover, the positive phase of the EU  
48 pattern in 2016 favored downward motions and weaker convergences of moisture and thus resulted in high air  
49 temperatures and a dry atmosphere in North China (Li et al., 2018).

50 High concentrations of ground-level ozone ( $O_3$ ) are frequently observed together with dry-hot air and intense  
51 solar radiation because photochemical reactions are accelerated under such meteorological conditions (Pu et al.,  
52 2017). The large-scale atmospheric circulations associated with high- $O_3$ -related meteorology in North China  
53 appeared as the positive phase of the EU pattern (Yin et al., 2019, 2020a). The anomalous anticyclonic circulations  
54 over North China, as one active center of the EU pattern, induced significant descending air flows and thus  
55 efficient adiabatic heating and intense sunlight (Gong and Liao, 2019). Generally, numerous nitrogen oxides ( $NO_x$ )  
56 and volatile organic compounds (VOCs) are emitted by human activities and natural sources in North China  
57 (Zheng et al., 2018). These precursors of  $O_3$  react under high ultraviolet radiation and generate more  $O_3$  (Fix et  
58 al., 2018).

59 The variation in the EU pattern and its linkage with surface  $O_3$  in North China were both driven by preceding  
60 spring forcings (Zhang et al., 2018; Yin et al., 2019, 2020a). Arctic sea ice anomalies in spring were proven to be

61 closely related to the summer EU teleconnection pattern; these anomalies then influenced rainfall in China (Wu  
62 et al., 2009). Summer surface O<sub>3</sub> in North China closely linked to the variability in May sea ice over the Gakkel  
63 Ridge (Figure S1) and the bridge in atmosphere was the EU pattern (Yin et al., 2019, 2020a). However, this  
64 relationship between sea ice anomalies and EU pattern showed a decadal change from insignificant to significant  
65 after the mid-1990s (Yin et al., 2020a). The east-west dipole of spring snow cover anomalies in Eurasia was  
66 closely related to the East Asia summer monsoon by stimulating atmospheric responses such as the EU pattern  
67 (Yim et al., 2010). When building a seasonal prediction model of surface O<sub>3</sub>-related meteorology, the May snow  
68 cover in West Siberia was selected as a predictor and effectively increased the predictability (Yin et al., 2020b).  
69 However, the physical mechanisms linking O<sub>3</sub> and snow cover are still unclear.

70 Two open questions are as follows: (1) Have the links between the EU pattern and O<sub>3</sub>-related meteorology  
71 in North China changed over the decades? (2) What is the roles of snow cover anomalies on driving the above  
72 connection? This study aimed to answer these unrevealed questions and explain the associated physical  
73 mechanisms. The remainder of this paper is organized as follows. Section 2 describes the data and methods, and  
74 the decadal changes in relationships between climatic factors were analyzed in Section 3. The physical  
75 mechanisms driving the changes were proposed and explained in Section 4. The main conclusions and necessary  
76 discussion of the results are included in Section 5.

## 77 **2. Datasets and methods**

### 78 **2.1 data descriptions**

79 The global satellite-based dataset of monthly snow concentrations was provided by Rutgers University  
80 (Robinson et al., 1993). Based on the daily product of the Interactive Multisensor Snow and Ice Mapping System,  
81 monthly 89 × 89 grid cell arrays of snow data were generated. To examine the reliability of this reanalysis snow  
82 data, routine daily snow observations at meteorological stations were also used (Bulygina et al., 2011) and were  
83 downloaded from the website <http://meteo.ru/tech/aisori.php>. Considering the available timescale of the data, 421  
84 stations were selected to collect data for the time period of 1980–2012 after quality control. Monthly sea ice (SI)  
85 concentrations with a horizontal resolution of 1°×1° were downloaded from the Met Office Hadley Centre (Rayner  
86 et al., 2003) and these data are widely used in sea ice-related analysis.

87 The Modern-Era Retrospective analysis for Research and Applications version 2 (MERRA2) is a NASA  
88 atmospheric reanalysis in the satellite era using the Goddard Earth Observing System Model, Version 5 (GEOS-  
89 5) with its Atmospheric Data Assimilation System (ADAS). The meteorological fields data with a horizontal

90 resolution of 0.5° latitude by 0.625° longitude were taken from the MERRA2 dataset (Gelaro et al., 2017),  
 91 including the geopotential height (Z) at 500 hPa and wind at 850 hPa, surface air temperature (SAT) and wind,  
 92 area fraction of middle and low clouds, boundary layer height (BLH), air temperature at 200 hPa, surface incoming  
 93 shortwave flux, surface net shortwave radiation, surface net longwave radiation, surface sensible heat flux, surface  
 94 latent heat flux and precipitation. These monthly mean MERRA2 data spanning from 1980 to 2018 were derived  
 95 from the Goddard Earth Sciences Data and Information Services Center. Besides, the abovementioned  
 96 atmospheric variables were also downloaded from the fifth generation European Center for Medium Range  
 97 Weather Forecasts (Copernicus Climate Change Service, 2017) to repeat the observational analyses and confirm  
 98 the robustness of the conclusions. Modified from Wang and He (2015), Yin et al. (2020a) calculated the summer  
 99 EU index as follows:

$$100 \quad EU = \left[ -1 \times \overline{Z500}_{(59-75^{\circ}\text{N}, 66-100^{\circ}\text{E})} + \overline{Z500}_{(40-54^{\circ}\text{N}, 105-128^{\circ}\text{E})} - 1 \times \overline{Z500}_{(27-33^{\circ}\text{N}, 126-137^{\circ}\text{E})} \right] / 3$$

101 where Z500 represents the geopotential height at 500 hPa and overbars denote the area average.

102 Ground-level O<sub>3</sub> concentrations have been observed since 2014 in China and are not sufficient to find long-  
 103 term standing climate relationships. In this study, we employed the ozone weather index (OWI) during 1980–  
 104 2018, which has been defined by Yin et al. (2019; 2020b) and was proven to be a comprehensive and effective  
 105 index determining the maximum daily average 8-h concentration of ozone (MDA8 O<sub>3</sub>). The correlation coefficient  
 106 between the observed MDA8 and daily OWI was 0.61 for the period 2007-2017 (Yin et al., 2019). The formula  
 107 for OWI in North China is as follows:

$$108 \quad OWI = \text{normalized V10mI} + \text{normalized BI} - \text{normalized PI} + \text{normalized DTI}.$$

109 where the V10mI is the area-averaged meridional wind at 10 m (35°–50°N, 110°–122.5°E), the BI is the area-  
 110 averaged boundary layer height (37.5°–47.5°N, 112.5°–120°E), the PI is the area-averaged precipitation (37.5°–  
 111 42.5°N, 112°–127.5°E), and the DTI is the area-averaged difference between the temperature at the surface  
 112 (37.5°–47.5°N, 110°–122.5°E) and at 200 hPa (37.5°–50°N, 110°–127.5°E). The normalized process is to divide  
 113 the anomaly by the standard deviation. These meteorological factors were selected based on their physicochemical  
 114 impacts on MDA8 O<sub>3</sub> that were summarized in Figure S2. For example, (1) anomalous southerlies (expressed by  
 115 V10mI) transported O<sub>3</sub> precursors from Yangtze River Delta and superposed them with the local high emissions  
 116 in North China (Yin et al., 2019; Gong et al., 2020); (2) More precipitation indicated more cloud cover and stronger  
 117 efficiency of sunlight blocking (–PI); (3) Cooler high-level troposphere corresponded to anticyclonic anomalies  
 118 and sunny sky, and warmer surface air and higher BLH resulted in active natural emissions of precursors and

119 photochemical reaction (DTI, BI).

## 120 **2.2 GEOS-Chem simulations**

121 To verify the statistical physical mechanisms and fill the gap between OWI and MDA8 O<sub>3</sub>, numerical  
122 simulations based on the nested version of global 3-D chemical transport model (GEOS-Chem) were designed  
123 and carried out. The GEOS-Chem model includes fully coupled O<sub>3</sub>-NO<sub>x</sub>-hydrocarbon and aerosol chemistry with  
124 more than 80 species and 300 reactions (Bey et al., 2001), and is driven by the MERRA2 meteorological data with  
125 0.5°×0.625° horizontal resolution and 47 vertical levels over nested grid over Asia (11°S–55°N, 60°E–150°E).  
126 The simulated ozone concentrations and the mass fluxes of ozone were calculated during the GEOS-Chem  
127 simulations. Now there are six major components (i.e., chemical reaction, transport, PBL mixing, convection,  
128 emissions and dry deposition, wet deposition) implemented for the budget diagnostics in GEOS-Chem model.  
129 Because non-local planetary boundary layer (PBL) mixing was used in the simulation, the emissions and dry  
130 deposition trends below the PBL were included within the mixing (Holtslag et al., 1993). Compared with other  
131 terms, the value of wet deposition was extremely small, so it was not considered in this study (Liao et al., 2006).  
132 Consequently, the major physical-chemical processes connected with meteorological conditions included the  
133 chemical reaction, transport, PBL mixing, convection and their sum within the PBL.

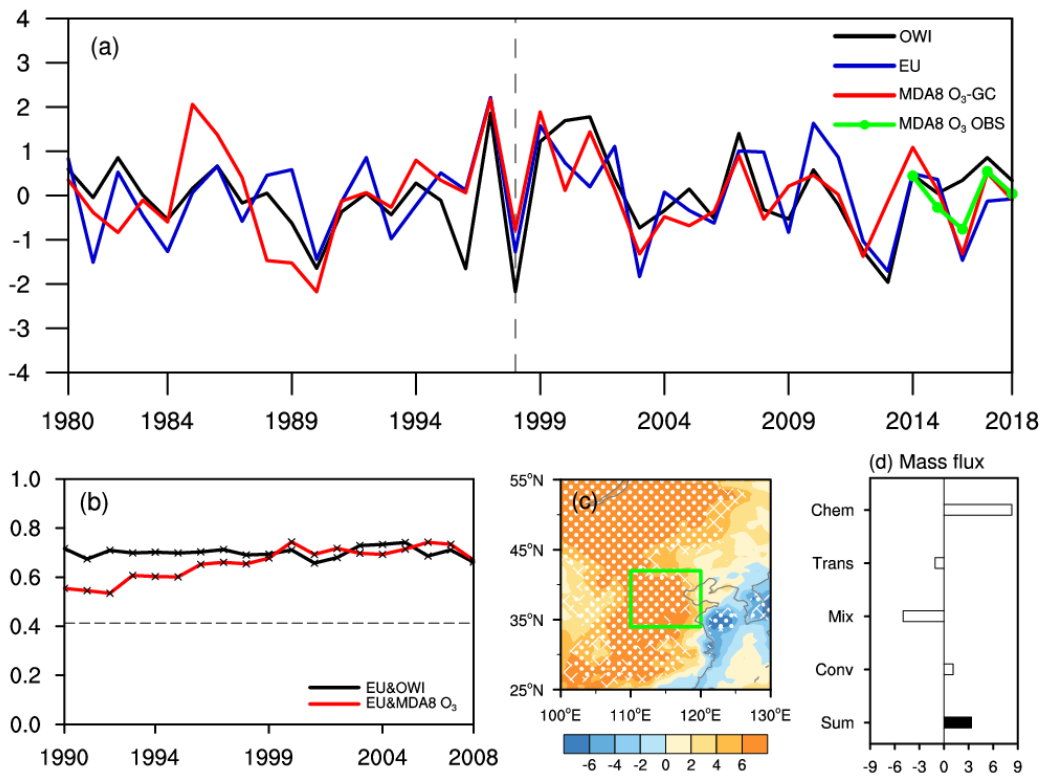
134 In this study, the GEOS-Chem model was driven by changing meteorological conditions during 1980–2018  
135 but with fixed anthropogenic emissions (MIX emission inventory in 2010) including from industry, power,  
136 residential and transportation sectors (Li et al., 2017); therefore, the interannual variations in MDA8 O<sub>3</sub> were  
137 mainly caused by meteorological anomalies. The simulated MDA8 O<sub>3</sub> were analyzed in two ways depending on  
138 two indexes (e.g., the years with the highest indexes minus those with the lowest indexes). The first composite  
139 was designed to investigate the sustaining impacts of the EU pattern on MDA8 O<sub>3</sub> in North China (EX<sub>EU</sub>) and the  
140 differences of simulated results between six highest and six lowest EU index years were calculated during 1980–  
141 2018. The second composite attempted to verify the changing influences of April-May (AM) snow cover on  
142 MDA8 O<sub>3</sub> (EX<sub>SC</sub>). The EX<sub>SC</sub> was executed in two separate periods: 1980–1998 and 1999–2018. In each sub-  
143 period, the simulated MDA8 O<sub>3</sub> was composited between the three lowest and three highest years of snow cover  
144 anomaly values.

## 145 **3. Changing connection between OWI and SC<sub>ws</sub>**

146 MDA8 O<sub>3</sub> highly correlated with the meteorological conditions. Yin et al. (2019) developed an index termed  
147 OWI to simulate the O<sub>3</sub> variations in North China (see Section 2.1) and largely extended the study period of O<sub>3</sub>  
148 pollution. Although the calculations of OWI were constructed based on the datasets from 2006–2016 in a regional

149 background air-monitoring station (located at 40.7°N, 117.1°E; and 293.3ma.m.s.l), it is evident that OWI stably  
150 reproduced the interannual variation in observed MDA8 O<sub>3</sub> in North China from 2014 to 2018 (green line in  
151 Figure 1a). Thus, the summer-mean OWI can be used to indicate the joint effects of O<sub>3</sub>-related meteorology in the  
152 interannual time scale. Furthermore, GEOS-Chem model was driven by meteorological conditions from 1980 to  
153 2018 with a fixed emission level. The simulated MDA8 O<sub>3</sub> showed similar interannual variations with the  
154 observations during 2014–2018 after removal of the linear trend (Figure S3), indicating good performances of our  
155 GEOS-Chem simulations. The MDA8 O<sub>3</sub> from GEOS-Chem mainly reflects the impacts of meteorological  
156 variability on surface O<sub>3</sub> via modulating the dispersions, photochemical productions and meteorology-emission  
157 interactions (Dang et al., 2020). The correlation coefficient between the observed JJA-mean OWI and simulated  
158 MDA8 O<sub>3</sub> was 0.6 from 1980 to 2018 (above the 99% confidence level) and the 21-yr running correlation  
159 coefficients maintained around 0.7 (Figure S4). The extreme OWI anomalies in 1990, 1997–1999, 2007, 2014  
160 and 2017 were also consistent with the results of the GEOS-Chem simulations (Figure 1a). Therefore, the observed  
161 OWI agreed with simulated MDA8 O<sub>3</sub> and successfully reflected the variation in O<sub>3</sub>-related meteorology and its  
162 impacts on O<sub>3</sub> pollution in North China.

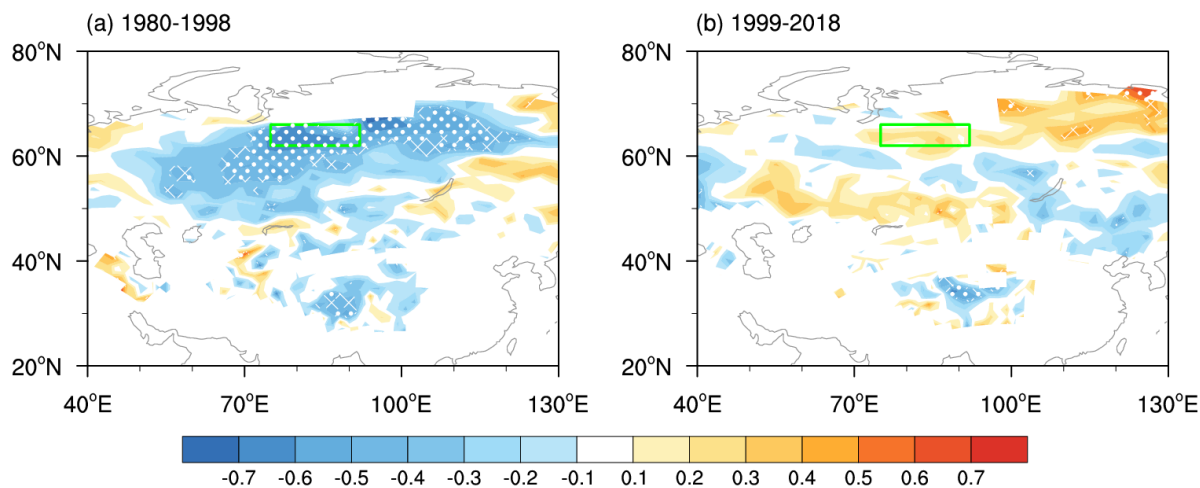
163 As aforementioned, the positive phase of the EU pattern was found to have a close relationship with the  
164 interannual variations in the OWI (Yin et al., 2019); the correlation coefficient was 0.65 from 1980 to 2018 after  
165 detrending (Figure 1a). In the 13 years when OWI reached extreme values (i.e.,  $|\text{OWI}| > 1 \times \text{standard deviation}$ ),  
166 the EU pattern also showed large values (i.e.,  $|\text{EU}| > 0.8 \times \text{standard deviation}$ ) in 8 years, accounting for 62% of  
167 the larger OWI anomalies. The correlation coefficient between the EU index and simulated MDA8 O<sub>3</sub> (i.e., 0.56)  
168 also exceeded the 99% confidence level during 1980–2018. In the EX<sub>EU</sub> experiment, the simulated MDA8 O<sub>3</sub>  
169 values in the six years with the highest and the six years with the lowest EU indexes were composited (highest  
170 minus lowest). Because emissions fixed, the significantly positive anomalies of MDA8 O<sub>3</sub> in Figure 1c resulted  
171 from different phases of the EU teleconnection and verified the impacts of the EU pattern on O<sub>3</sub> pollution in North  
172 China. The physical-chemical processes of ozone production in GEOS-Chem simulations were analyzed. When  
173 the EU pattern was at high positive phase, chemical reactions had large positive values. Although transport and  
174 mixing had negative values, the sum of all physical-chemical processes was 8.27 Tons d<sup>-1</sup>, resulting more O<sub>3</sub>  
175 (Figure 1d). Furthermore, the 21-year running correlation coefficient between the EU index and observed OWI  
176 (simulated MDA8 O<sub>3</sub>) remained at approximately 0.7 (0.6) and was persistently above the 99% confidence level  
177 (Figure 1b), indicating that the connections between the EU pattern and O<sub>3</sub>-related meteorology in North China  
178 did not change over time.



179

180 **Figure 1.** (a) The normalized variation in JJA-mean OWI (black), EU index (blue), simulated MDA8 O<sub>3</sub> (red) from 1980 to  
 181 2018 and observed MDA8 O<sub>3</sub> (green) from 2014 to 2018 after detrending. (b) The 21-year sliding correlation coefficients  
 182 between simulated MDA8 O<sub>3</sub> (red), OWI (black) and EU. The black dotted line (crosses) indicates (exceeded) the 95%  
 183 confidence level. (c) Composite difference of the simulated MDA8 O<sub>3</sub> (unit:  $\mu\text{g m}^{-3}$ ) in summer between the six highest and  
 184 the six lowest EU index years from 1980 to 2018. The white dots (hatching) indicate that the difference was above the 95%  
 185 (90%) confidence level ( $t$  test). The green box represents the location of North China. (d) Composite difference of the mass  
 186 fluxes of summer ozone (unit:  $\text{tons d}^{-1}$ ) from the GEOS-Chem between the six highest and the six lowest EU years from 1980  
 187 to 2018. The left axis is the name of the physical-chemical processes: chemical reaction (Chem), transport (Trans), PBL mixing  
 188 (Mix), convection (Conv) and their sums (Sum).

189 The 39-yr correlation coefficients between AM-mean Eurasia snow cover and summer mean OWI were  
 190 weakly negative (figure omitted). However, they were significantly negative in West Siberia and Central Siberia  
 191 during 1980–1998 (P1, Figure 2a) and these correlations disappeared during the period of 1999–2018 (P2, Figure  
 192 2b). The availability of snow data in three regions (i.e., West Siberia, Central Siberia and the northern area to  
 193 Baikal) was verified before confirming the key region of snow cover anomalies. Judging from the spatial and  
 194 temporal correlation analysis, the reanalysis data of snow cover provided by Rutgers University agreed well with  
 195 the site observations in West Siberia ( $62^{\circ}$ – $66^{\circ}\text{N}$ ,  $75^{\circ}$ – $92^{\circ}\text{E}$ ) from 1980 to 2012 (Figure S5). Thus, the regional  
 196 mean of AM-mean Eurasian snow cover in this region was defined as the  $\text{SC}_{\text{WS}}$ , which was also significantly and  
 197 negatively correlated with the summer EU pattern (Figure S6). Furthermore, as pointed by Yin et al. (2020a), sea  
 198 ice anomalies in the Gakkel Ridge ( $\text{SI}_{\text{GR}}$ ,  $82^{\circ}$ – $88^{\circ}\text{N}$ ,  $0^{\circ}$ – $80^{\circ}\text{E}$ , Figure S1) also bridged the summer EU and OWI.

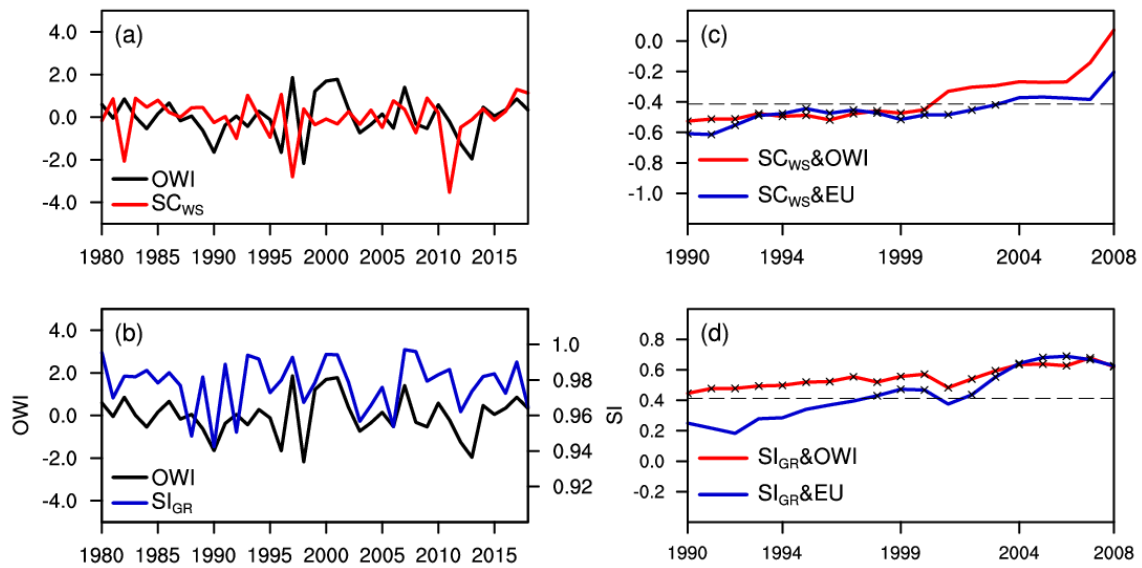


199

200 **Figure 2.** The correlation coefficients between the JJA-mean OWI and AM-mean snow cover (a) from 1980 to 1998 and (b)  
 201 from 1999 to 2018. The white dots (hatching) indicate that the correlation coefficients exceeded the 95% (90%) confidence  
 202 level ( $t$  test). The green box represents the key area used to calculate the SC<sub>sw</sub> index. The linear trend is removed.

203 During 1980–2018, the correlation coefficients between OWI and the above two external forcings were 0.5  
 204 ( $SI_{GR}$ , significant at the 99% confidence level) and  $-0.21$  ( $SC_{WS}$ , insignificant at the 95% confidence level),  
 205 respectively (Figure 3 a, b). We also checked the 21-year running correlation coefficients between each forcing  
 206 and OWI in Figure 3c-d, both of which showed decadal changes and independent with the choice of running time  
 207 window (Figure omitted). The correlation between OWI and  $SC_{WS}$  was significant ( $-0.68$ , above the 99%  
 208 confidence level) during P1 and became insignificant ( $0.20$ ) during P2 (Figure 3c). Oppositely, the correlation  
 209 with  $SI_{GR}$  enhanced from  $0.4$  in P1 to  $0.62$  in P2 (Figure 3d). After removing the signal of El Niño-Southern  
 210 Oscillation (ENSO), these correlation coefficients almost unchanged. Interestingly, the connections between these  
 211 two preceding factors and the EU pattern illustrated similar decadal changes (Figure 3 c, d). That is, the correlation  
 212 between EU and  $SC_{WS}$  was only significant ( $-0.62$ ) in the former period; however, the correlation between EU  
 213 and  $SI_{GR}$  was only significant ( $0.61$ ) after the mid-1990s (Figure 3 c, d). Furthermore, the  $SI_{GR}$  and  $SC_{WS}$  were  
 214 mutually independent because the 21-year running correlation coefficient between them was maintained at a low  
 215 level (Figure S7). Therefore, we speculated that the impacts of the summer EU pattern on ground-level  $O_3$   
 216 pollution in North China were robust and long-standing (Figure 1b). However, the preceding factors inducing the  
 217 EU pattern to influence the  $O_3$  pollution in North China changed from  $SC_{WS}$  in P1 to  $SI_{GR}$  in P2 (Figure 3 c, d).

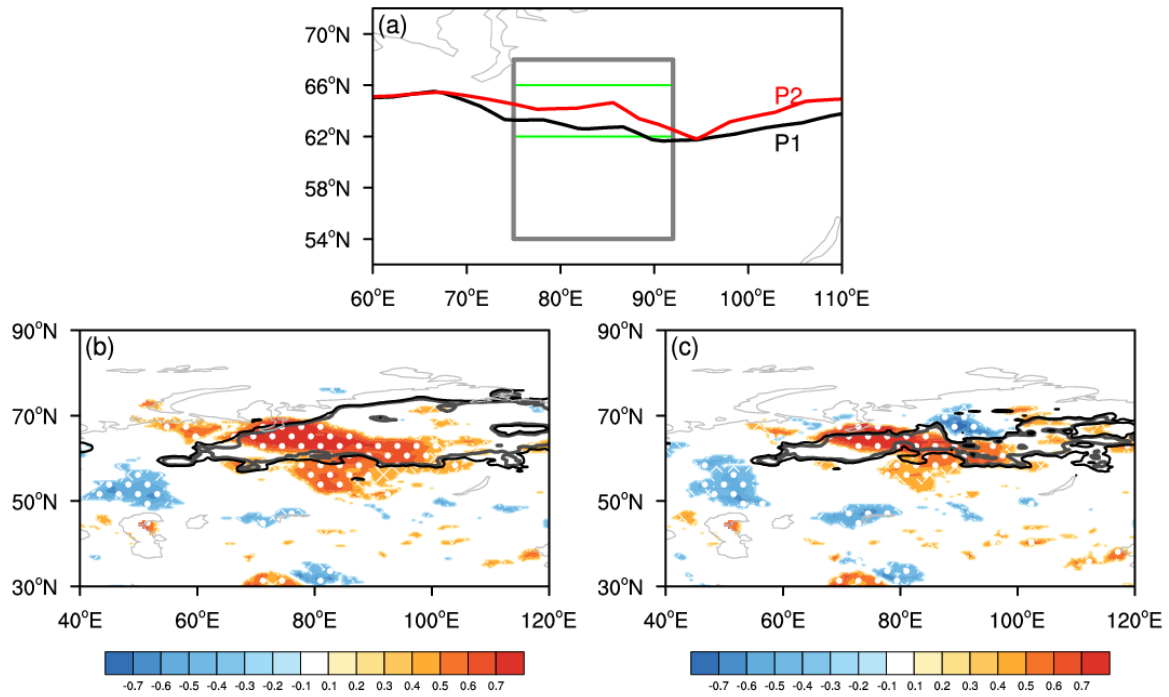




218  
 219 **Figure 3.** The normalized variation in (a) OWI (black) and SC<sub>WS</sub> (red), (b) OWI (black) and SI<sub>GR</sub> (blue) from 1980 to 2018  
 220 after detrending. The 21-year sliding correlation coefficients between (c) SC<sub>WS</sub> and OWI (red), EU (blue), (d) SI<sub>GR</sub> and OWI  
 221 (red), EU (blue). The black dotted line (crosses) indicates (exceeded) the 95% confidence level. The linear trend is removed.

#### 222 4. Physical mechanisms

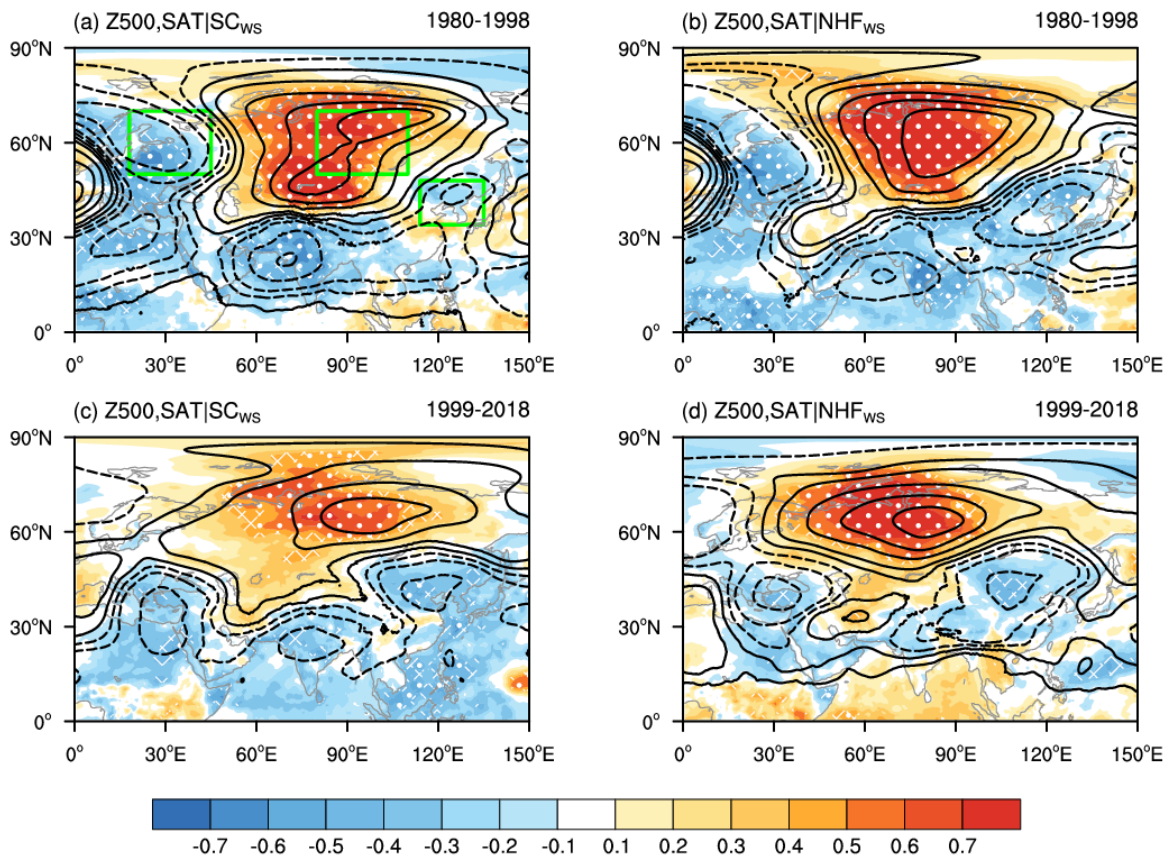
223 The physical mechanisms of how to achieve the impacts of SC<sub>WS</sub> on surface O<sub>3</sub> pollution in North China is  
 224 still a new question to the best of our knowledge. As an efficient climate forcing, the snow cover anomalies could  
 225 stimulate synchronous responses in the atmosphere by changing albedo and hydrological effects and could then  
 226 impact the atmosphere in the following seasons (Cohen and Rind, 1991). In April and May, the snow at high  
 227 latitudes began to melt and had obvious interannual variations, as shown by both the observations and the  
 228 reanalysis data (Figure S5). Generally, lower albedo, associated with less snow cover, meant that the land/snow  
 229 surface reflected less solar radiation and resulted in higher SAT. Warmer surfaces produce stronger longwave  
 230 radiation and heat the local atmosphere from the surface to the mid-troposphere (Chen et al., 2003; Chen et al.,  
 231 2016). Moreover, the changing local soil moisture enhanced the surface heat flux and thus resulted in higher SAT  
 232 and atmospheric temperatures (Zhang et al., 2017). Finally, the warmed thermal conditions in the atmosphere  
 233 enhanced the local 1000–500 hPa thickness and represented positive anomalies of Z500 (Chen et al., 2003; Halder  
 234 and Dirmeyer, 2017). Compared to P1, the south edge of the area with high concentrations of snow (>85%) in late  
 235 spring shifted northward by approximately 2° in latitude during P2 (Figure 4a). Similarly, the significant changes  
 236 in radiation flux (shortwave + longwave) and heat flux (latent + sensible) also moved northward in P2 relative to  
 237 P1 (Figure 4 b, c). We speculated that this northward movement of effective snow cover, accompanied by shifts  
 238 in net heat flux, possibly contributed to the changing relationship between the SC<sub>WS</sub> and OWI.



239

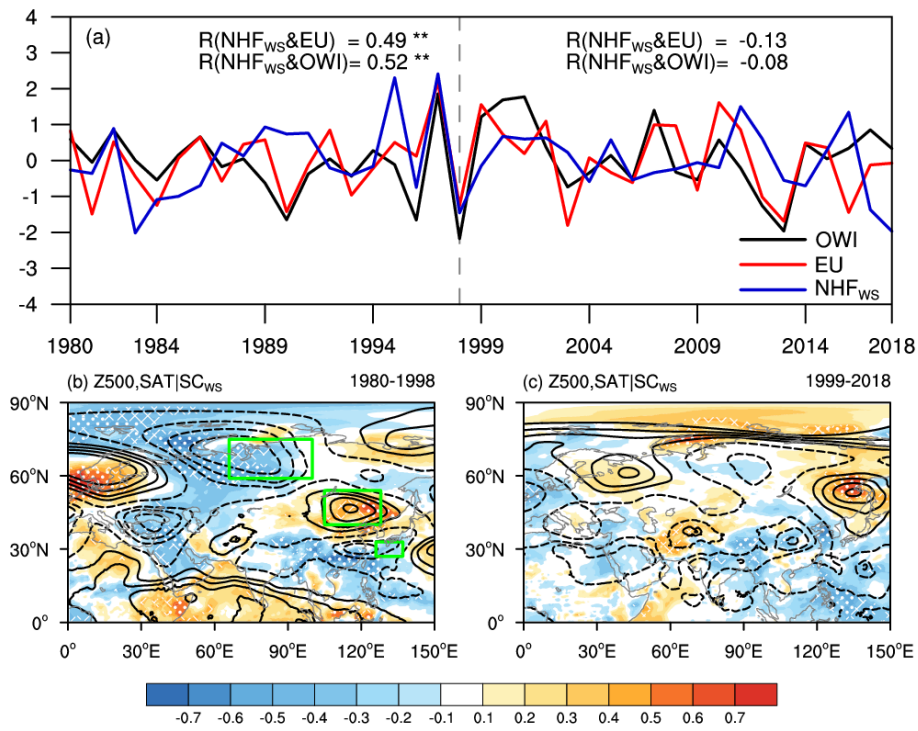
240 **Figure 4.** (a) The south edge of the 85% snow cover concentration during 1980–1993 (black) and during 2004–2018 (red).  
 241 The gray (green) box represents the key area used to calculate the NHF<sub>WS</sub> (SC<sub>sw</sub>) index. The correlation coefficients between  
 242 the SC<sub>WS</sub> × -1 and (b) surface net radiation flux (shortwave+longwave) and (c) surface net heat flux (latent+sensible) are  
 243 displayed during 1980–1998 (shading) and 1999–2018 (contour). White dots (hatching) indicate that the correlation  
 244 coefficients during P1 exceeding the 95% (90%) confidence level (*t* test). The gray (black) contours represent the correlation  
 245 coefficients during P2 exceeding the 95% (90%) confidence level. The linear trend is removed.

246 The local responses of geopotential height in the mid-troposphere induced by negative anomalies of the SC<sub>WS</sub>  
 247 illustrated decadal changes; that is, the significant correlation coefficients between SC<sub>WS</sub> × -1 and Z500, as well  
 248 as SAT, were distributed more southward and were stronger in P1 (Figure 5a) than in P2 (Figure 5c). For  
 249 convenience, the roles of radiation and heat flux (shortwave + longwave + latent + sensible) were considered  
 250 together as net heat flux (Zhang et al., 2017), which was averaged over West Siberia (54°–68°N, 75°–92°E) and  
 251 defined as NHF<sub>WS</sub>. It was evident that the atmospheric responses associated with the NHF<sub>WS</sub> agreed well with  
 252 those of less SC<sub>WS</sub> (Figure 5 b, d). That is, the enhanced net heat flux related to decreased snow cover in West  
 253 Siberia heated the above atmosphere and resulted in local warmer SAT and anticyclonic circulations in the mid-  
 254 troposphere during P1 (Figure 5 a, b). In addition, cyclonic responses can be found on the left and right sides of  
 255 the aforementioned anticyclonic anomalies in April-May (Figure 5 a, b). However, similar to the radiation and  
 256 heat flux in Figure 4 b-c, the atmospheric responses were distributed more northward and were weaker during P2  
 257 than during P1 (Figure 5 c, d).



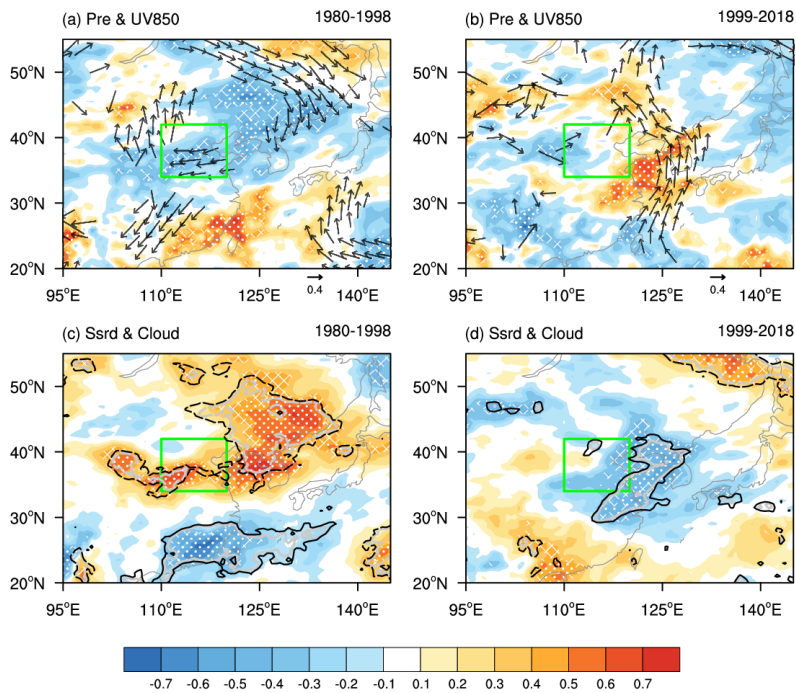
258  
 259 **Figure 5.** The correlation coefficients between the  $SC_{ws} \times -1$  (a, c),  $NHF_{ws}$  (b, d) and surface air temperature (shading) and  
 260 geopotential height at 500 hPa (contour) from 1980 to 1998 (a, b) and from 1999 to 2018 (c, d). The white dots (hatching)  
 261 indicate that the correlation coefficients in shading exceeded the 95% (90%) confidence level ( $t$  test). The green boxes represent  
 262 the anomalous cyclonic or anticyclonic centers in AM. The linear trend is removed.

263 The AM-mean  $NHF_{ws}$  showed significantly positive correlations with both the summer-mean EU (0.49) and  
 264 OWI (0.52) during P1 (Figure 6a, S8a). After removing the ENSO signal, these correlated relationships almost  
 265 showed no difference. Furthermore, the “+” anomalous atmospheric centers in April-May (green boxes in  
 266 Figure 5a) had significantly positive correlations with the summer EU pattern (CC=0.45, above the 95%  
 267 confidence level). The atmospheric anomalies stimulated by negative  $SC_{ws}$  could appear as positive phases of the  
 268 EU pattern in JJA during P1 (Figure 6b, S8a). As one center of the EU pattern, the anticyclonic anomalies over  
 269 North China were significant in the mid- and lower-troposphere (Figure 6b, 7a) and resulted in clear skies (Figure  
 270 7c). Sinking heating, intense sunlight (Figure 7c) and less precipitation (correspondingly more cloud and weaker  
 271 ultraviolet radiations, Figure 7a) resulted in beneficial environments for the natural emissions of  $O_3$  precursors  
 272 (Lu et al., 2019) and photochemical reactions (Pu et al., 2017). Differently, the northward and weaker atmospheric  
 273 responses in April-May were almost dispersed in summer (Figure 6c, S8b) and had little impacts on the local OWI  
 274 in North China (Figure 7 b, d) during P2, which were consistent with the insignificant correlations between the  
 275  $NHF_{ws}$  and the EU (OWI) (Figure 6a).



276  
277  
278  
279  
280  
281  
282  
283

**Figure 6.** (a) The normalized variation in the JJA OWI (black), JJA EU index (red) and AM NHF<sub>ws</sub> (blue) from 1980 to 2018 after detrending. The numbers represent the correlation coefficients between the NHF<sub>ws</sub> and EU, OWI during 1980–1998 and 1999–2018, respectively. Two asterisks indicate that the correlation coefficients exceeded the 95% confidence level. The correlation coefficients between SC<sub>ws</sub> × -1 and JJA surface air temperature (shading) and geopotential height at 500 hPa (contour) from 1980 to 1998 (b) and from 1999 to 2018 (c). The white dots (hatching) indicate that the correlation coefficients with surface air temperature exceeded the 95% (90%) confidence level (*t* test). The green boxes represent the key areas used to calculate the EU index. The linear trend is removed.

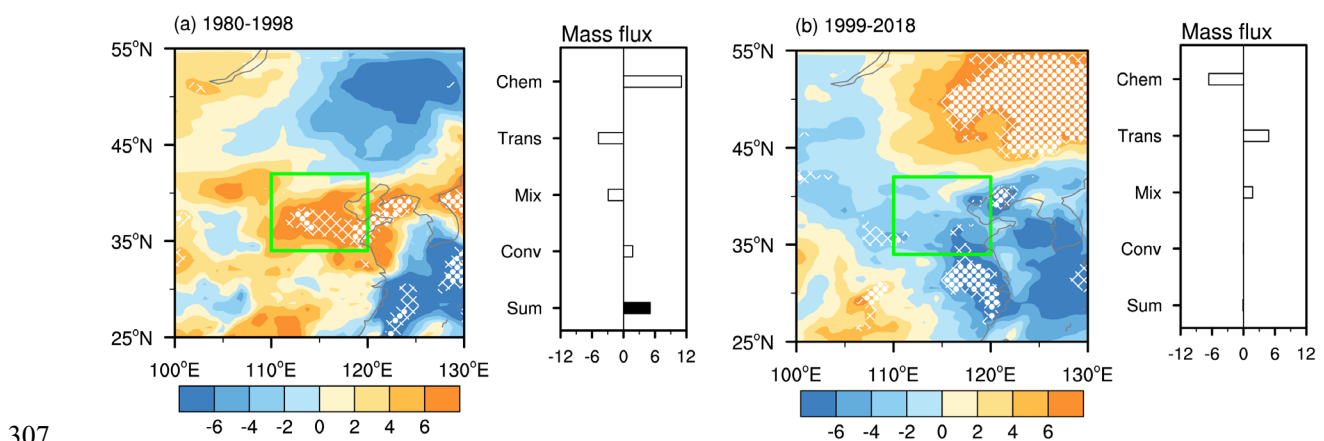


284  
285  
286  
287

**Figure 7.** The meteorological conditions associated with the SC<sub>ws</sub> × -1. (a, b) The correlation coefficients between SC<sub>ws</sub> × -1 and precipitation (shading) and wind at 850 hPa (arrow); (c, d) surface incoming shortwave flux (shading), and the sum of low and medium cloud cover (contour) from 1980 to 1998 (a, c) and from 1999 to 2018 (b, d). The white dots (hatching) indicate

288 that the correlation coefficients represented with shading exceeded the 95% (90%) confidence level (*t* test). The gray (black)  
 289 contours exceeded the 95% (90%) confidence level. The green boxes represent the location of North China. The linear trend  
 290 is removed.

291 In the EX<sub>SC</sub> experiment, the simulated MDA8 O<sub>3</sub> and mass fluxes of ozone were composited (three lowest  
 292 SC<sub>WS</sub> minus highest) during P1 and P2, respectively. During P1, the composited results (with fixed emissions)  
 293 were significantly positive (Figure 8a) and were in good agreement with the proposed mechanisms (i.e., less snow  
 294 cover in West Siberia resulted in severe surface O<sub>3</sub> pollution in North China). The responses of MDA8 O<sub>3</sub> pollution  
 295 in North China were insignificant during P2 (Figure 8b) and were also consistent with both weak impacts in this  
 296 period and changing relationships. Mass balance of ozone are jointly determined by four processes (i.e., chemistry,  
 297 transport, PBL mixing and convection) which could be isolated by the GEOS-Chem model. During P1, the  
 298 composite results of chemical reaction had large positive values (11.05 Tons d<sup>-1</sup>) (Figure 8a), indicating that the  
 299 dry-hot meteorological conditions were conducive to produce more O<sub>3</sub>. Anomalous anticyclonic circulations  
 300 located above the North China region resulted in downward air flow that may bring the ozone from the  
 301 stratosphere to surface. Hence, the value of convection was also positive. The values of transport and mixing were  
 302 negative (Figure 8a), but the sum of all processes was positive, indicating the ozone concentrations in North China  
 303 would increase. However, the composite results of chemical, transport and mixing were opposite (Figure 8b)  
 304 during P2 compared with P1. Meanwhile, the values of convection and the sum were extremely close to zero  
 305 (Figure 8b), indicating that there were little impacts on ozone in North China when the SC<sub>WS</sub> was low during P2.  
 306 The composite results of mass fluxes were well agreement with the previous conclusion.

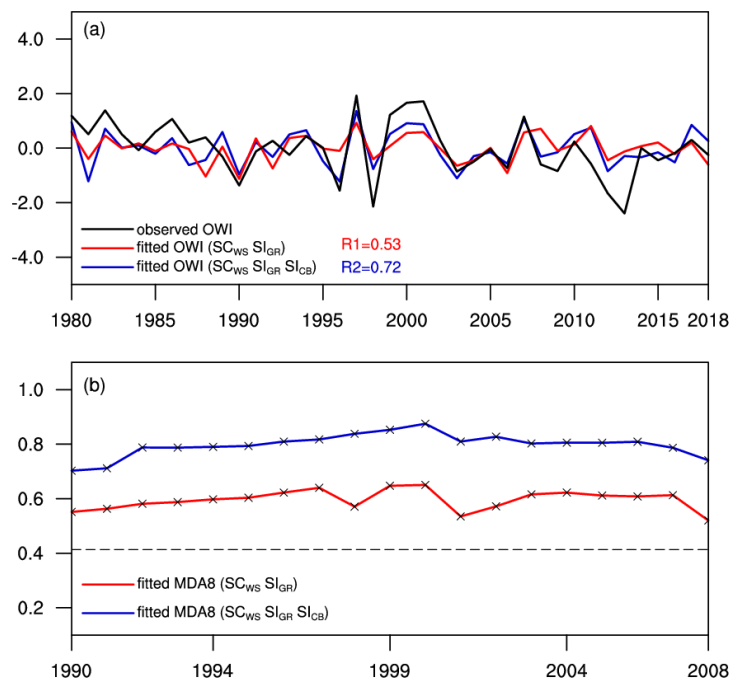


308 **Figure 8.** Composite difference of the summer MDA8 O<sub>3</sub> (unit:  $\mu\text{g m}^{-3}$ ) simulated by the GEOS-Chem model between the  
 309 three lowest and the three highest SC<sub>WS</sub> years (a) from 1980 to 1998 and (b) from 1999 to 2018. The white dots (hatching)  
 310 indicate that the difference was above the 95% (90%) confidence level (*t* test). The green boxes represent the location of North  
 311 China. The bar chart on the right is the composite difference of the summer mass fluxes of ozone (unit: tons d<sup>-1</sup>) during each  
 312 periods. The left axis is the name of the physical-chemical processes: chemical reaction (Chem), transport (Trans), PBL mixing  
 313 (Mix), convection (Conv) and their sums (Sum). The results were calculated within the planetary boundary layer.

## 314 5. Conclusions and discussion

315 In this study, the April-May snow cover in West Siberia was newly proposed as a preceding climate driver  
316 that influenced the surface O<sub>3</sub>-related meteorology in North China during 1980–1998, and the associated physical  
317 mechanisms were also explained by comparing the periods before and after the mid-1990s. Accompanying the  
318 northward shift of dense snow cover, the associated radiation and heat flux also retreated toward the polar region  
319 during 1999–2018 (Figure 4); thus, the induced atmospheric anomalies were located northward in April-May and  
320 disappeared in summer (Figure 5 c, d). However, in the period of 1980–1998, the positive phase of the EU pattern  
321 in summer could be stimulated by negative anomalies of snow cover (mainly by enhanced net heat flux) in West  
322 Siberia (Figure 6). Consequently, hot-dry air and intense solar radiation under anomalous anticyclonic circulations  
323 not only enhanced the natural emissions of O<sub>3</sub> precursors but also promoted photochemical reactions to produce  
324 more O<sub>3</sub> near the surface (Figure 7, 8). To enhance the robustness of this study, the ERA5 reanalysis data were  
325 also employed to reproduce the observational analyses. As shown in Figure S9, identical results were obtained  
326 and confirmed.

327 The linkage between the EU pattern and MDA8 O<sub>3</sub> was robust, which bridged the SC<sub>WS</sub> and OWI in the  
328 period of 1980–1998 but connected the SI<sub>GR</sub> and OWI after the mid-1990s. In Figure 9, the OWI were regressed  
329 by SC<sub>WS</sub> and SI<sub>GR</sub> from 1980–2018. The 21-year running correlation coefficient between the OWI and the fitted  
330 values stably maintained around 0.6 and indicated that these two preceding factors almost introduced the full  
331 impacts of the EU pattern (Figure 1b) over the whole period. Generally, the decadal changes in the climate drivers  
332 influences the stability of the predictability. It is evident that our results overcame this problem and deepened the  
333 understanding of variations in summer O<sub>3</sub> from the climate perspective. Yin et al. (2020a) also found that the sea  
334 ice anomalies over the Canada Basin and the Beaufort Sea (Figure S1) also stimulated a Rossby-wave-like train  
335 propagating through the North Pacific to influence the variability in the OWI in North China. When we added  
336 these sea ice anomalies into the regressions, the fitting performance was visibly improved because the 21-year  
337 running correlation coefficient was elevated to approximately 0.8 with OWI, as seen in Figure 9b.



338

339 **Figure 9.** (a) The variation in the JJA-mean observed OWI (black), the fitted OWI-1 (by the  $SC_{WS}$  and  $SI_{GR}$ , red), and the  
 340 fitted OWI-2 (by the  $SC_{WS}$ ,  $SI_{GR}$  and  $SI_{CB}$ , blue) from 1980 to 2018 after detrending. (b) The 21-year sliding correlation  
 341 coefficients between observed OWI and fitted OWI-1 (red), fitted OWI-2 (blue). The black dotted line (crosses) indicates  
 342 (exceeded) the 95% confidence level.

343 The concentrations of surface  $O_3$  have been extensively measured since 2014 in China; this time scale cannot  
 344 support the study of the interannual-decadal variability in  $O_3$  pollution. In this study, we used two datasets, i.e.,  
 345 the ozone weather index and the  $O_3$  concentrations simulated by GEOS-Chem, to focus on the impacts of climate  
 346 variability on surface  $O_3$  in North China. Although the feasibility of these datasets was strictly examined, there  
 347 were still gaps between the real variations in  $O_3$  and the variations in these two substitutions; this discrepancy  
 348 requires further research. Moreover, the climate-chemistry coupled model need be used to verify the role of snow  
 349 cover on ozone pollution in North China in further studies. Furthermore, there is no doubt that anthropogenic  
 350 emissions are the fundamental drivers of  $O_3$  pollution, which has been investigated in many previous studies (Li  
 351 et al., 2018; Li et al., 2019; Dang et al., 2020). After removal of the linear trend, the signals of climate warming  
 352 in the atmosphere were also eliminated, which allowed us to focus on the interannual variations. In addition, the  
 353 decrease in haze aerosols was also proven to be an effective contributor to recent interannual variations in  $O_3$   
 354 concentrations (Li et al., 2019), which were not involved in our study and need further attentions.

355 **Data Availability.** Hourly O<sub>3</sub> concentration data can be downloaded from <https://quotsoft.net/air/> (Ministry of  
356 Environmental Protection of China, last accessed on 8 November 2020). Sea ice concentration data are from  
357 <https://www.metoffice.gov.uk/hadobs/hadisst/data/download.html> (Met Office Hadley Centre, 2020). Snow cover  
358 data can be downloaded from Rutgers University at <http://climate.rutgers.edu/snowcover/> (Rutgers University,  
359 2020). The observed snow data from meteorological stations are available at <http://meteo.ru/tech/aisori.php>. The  
360 monthly mean MERRA2 reanalysis datasets are available at <https://disc.gsfc.nasa.gov/datasets?page=1> (last  
361 access: 21 March 2021). The monthly mean ERA5 reanalysis datasets are available at  
362 <https://cds.climate.copernicus.eu/cdsapp#!/home> (Copernicus Climate Change Service, last accessed on 9  
363 November 2020).

#### 364 **Acknowledgements**

365 This research was supported by National Natural Science Foundation of China (91744311, 42088101, 41991283  
366 and 42025502).

#### 367 **Authors' contribution**

368 Wang H. J. and Yin Z. C. designed and performed researches. Wan Y. did the statistical analysis and implemented  
369 the GEOS-Chem simulations. Yin Z. C. prepared the manuscript with contributions from all co-authors.

#### 370 **Competing interests**

371 The authors declare no conflict of interest.



372 **References**

- 373 Bey, I., Jacob, D. J., Yantosca, R. M., Logan, J. A., Field, B., Fiore, A. M., Li, Q., Liu, H., Mickley, L. J., and  
374 Schultz, M.: Global modeling of tropospheric chemistry with assimilated meteorology: Model description and  
375 evaluation, *J. Geophys. Res.*, 106, 23073–23095, <https://doi.org/10.1029/2001JD000807>, 2001.
- 376 Bulygina, O. N., Groisman, P. Y., Razuvaev, V. N., and Korshunova, N. N.: Changes in snow cover characteristics  
377 over Northern Eurasia since 1966, *Environ. Res. Lett.*, 6, 045204, <https://doi.org/10.1088/1748-9326/6/4/045204>,  
378 2011.
- 379 Chen, H. S., Sun, Z. B., and Zhu, W. J.: The Effects of Eurasian Snow Cover Anomaly on Winter Atmospheric  
380 General Circulation Part II. Model Simulation, *Chinese J. Atmos. Sci (in Chinese)*., 27, 547–860,  
381 <https://doi.org/10.3878/j.issn.1006-9895.2003.03.02>, 2003.
- 382 Chen, S. F., Wu, R. G., and Liu, Y.: Dominant Modes of Interannual Variability in Eurasian Surface Air  
383 Temperature during Boreal Spring, *J. Climate*, 29, 1109–1125, <https://doi.org/10.1175/JCLI-D-15-0524.1>, 2016.
- 384 Cohen, J., and Rind, D.: The effect of snow cover on the climate, *J. Climate*, 4, 689–706,  
385 [https://doi.org/10.1175/1520-0442\(1991\)0042.0.CO;2](https://doi.org/10.1175/1520-0442(1991)0042.0.CO;2), 1991.
- 386 Dang, R. J., Liao, H., and Fu, Y.: Quantifying the anthropogenic and meteorological influences on summertime  
387 surface ozone in China over 2012–2017, *Sci. Total Environ.*, 754, 142394,  
388 <https://doi.org/10.1016/j.scitotenv.2020.142394>, 2020.
- 389 Copernicus Climate Change Service.: ERA5: fifth generation of ECMWF atmospheric reanalyses of the global  
390 climate Copernicus Climate Change Service Climate Data Store, 2017.
- 391 Fix, M. J., Cooley, D., Hodzic, A., Gilleland, E., Russell, B. T., Porter, W. C., and Pfister, G. G.: Observed and  
392 predicted sensitivities of extreme surface ozone to meteorological drivers in three US cities, *Atmos. Environ.*, 176,  
393 292–300, <https://doi.org/10.1016/j.atmosenv.2017.12.036>, 2018.
- 394 Gelaro, R., McCarty, W., Suarez, M. J., Todling, R., Molod, A., Takacs, L., Randles, C. A., Darmenov, A.,  
395 Bosilovich, M. G., Reichle, R., Wargan, K., Coy, L., Cullather, R., Draper, C., Akella, S., Buchard, V., Conaty, A.,  
396 da Silva, A. M., Gu, W., Kim, G. K., Koster, R., Lucchesi, R., Merkova, D., Nielsen, J. E., Partyka, G., Pawson, S.,  
397 Putman, W., Rienecker, M., Schubert, S. D., Sienkiewicz, M., and Zhao, B.: The Modern-Era Retrospective Analysis  
398 for Research and Applications, Version 2 (MERRA2), *J. Climate*, 30, 5419–5454, [https://doi.org/10.1175/jcli-d-](https://doi.org/10.1175/jcli-d-160758.1)  
399 160758.1, 2017.
- 400 Gong, C., and Liao, H.: A typical weather pattern for ozone pollution events in North China, *Atmos. Chem. Phys.*,  
401 19, 13725–13740, <https://doi.org/10.5194/acp-19-13725-2019>, 2019.
- 402 Gong, C., Liao, H., Zhang, L., Yue, X., Dang, R. J., and Yang, Y.: Persistent ozone pollution episodes in North  
403 China exacerbated by regional transport, *Environ. Pollut.*, 265, 115056, [https://doi.org/10.1016/j.envpol.2020.1](https://doi.org/10.1016/j.envpol.2020.115056)  
404 15056, 2020.
- 405 Gong, D. Y., Wang, S. W., and Zhu, J. H.: East Asian winter monsoon and Arctic oscillation, *Geophys. Res. Lett.*,  
406 28, 2073–2076, <https://doi.org/10.1029/2000GL012311>, 2001.

407 Halder, S., and Dirmeyer, P. A.: Relation of Eurasian Snow Cover and Indian Summer Monsoon Rainfall:  
408 Importance of the Delayed Hydrological Effect, *J. Climate*, 30, 1273–1289, <https://doi.org/10.1175/JCLI-D-16->  
409 0033.1, 2017.

410 Holtslag, A., and Boville, B. A.: Local versus nonlocal boundary layer diffusion in a global climate model, *J.*  
411 *Climate*, 6, 1825–1842, [https://doi.org/10.1175/1520-0442\(1993\)006<1825:LVNBLD>2.0.CO;2](https://doi.org/10.1175/1520-0442(1993)006<1825:LVNBLD>2.0.CO;2), 1993.

412 Li, H., Chen, H., Wang, H., Sun, J., and Ma, J.: Can Barents Sea Ice Decline in Spring Enhance Summer Hot  
413 Drought Events over Northeastern China? *J. Climate*, 31, 4705–4725, <https://doi.org/10.1175/JCLI-D-17-0429.1>,  
414 2018.

415 Li, K., Jacob, D. J., Liao, H., Shen, L., Zhang, Q., and Bates, K. H.: Anthropogenic drivers of 2013-2017 trends  
416 in summer surface ozone in China, *P. Natl. Acad. Sci. USA*, 116, 422–427,  
417 <https://doi.org/10.1073/pnas.1812168116>, 2019.

418 Li, M., Zhang, Q., Kurokawa, J. I., Woo, J. H., He, K., Lu, Z., Ohara, T., Song, Y., Streets, D. G., Carmichael, G.  
419 R., Cheng, Y., Hong, C., Huo, H., Jiang, X., Kang, S., Liu, F., Su, H., and Zheng, B.: MIX: a mosaic Asian  
420 anthropogenic emission inventory under the international collaboration framework of the MICS-Asia and HTAP,  
421 *Atmos. Chem. Phys.*, 17, 935-963, doi:10.5194/acp-17-935-2017, 2017.

422 Li, N., He, Q., Greenberg, J., Guenther, A., Li, J., Cao, J., Wang, J., Liao, H., Wang, Q., and Zhang, Q.: Impacts  
423 of biogenic and anthropogenic emissions on summertime ozone formation in the Guanzhong Basin, China, *Atmos.*  
424 *Chem. Phys.*, 18, 7489–7507, <https://doi.org/10.5194/acp-18-7489-2018>, 2018.

425 Li, Y., Sheng, L., Li, C., and Wang Y.: Impact of the Eurasian Teleconnection on the Interannual Variability of  
426 Haze-Fog in Northern China in January, *Atmosphere*, 10, 113, <https://doi.org/10.3390/atmos10030113>, 2019.

427 Liao, H., Chen, W. T., and Seinfeld, J. H.: Role of climate change in global predictions of future tropospheric  
428 ozone and aerosols, *J. Geophys. Res.-Atmos.*, 111, D12304, <https://doi.org/10.1029/2005JD006852>, 2006.

429 Lim, Y. K., and Kim, H. D.: Comparison of the impact of the Arctic Oscillation and Eurasian teleconnection on  
430 interannual variation in East Asian winter temperatures and monsoon, *Theor. Appl. Climatol.*, 124, 267–279,  
431 <https://doi.org/10.1007/s00704-015-1418-x>, 2016.

432 Liu, Y., and Chen, W.: Variability of the Eurasian teleconnection pattern in the Northern Hemisphere winter and  
433 its influences on the climate in China, *Chinese J. Atmos. Sci (in Chinese)*, 36, 423–432,  
434 [https://doi.org/10.2151/jmsj1965.77.2\\_495](https://doi.org/10.2151/jmsj1965.77.2_495), 2012.

435 Liu, Y., Wang, L., Zhou, W., and Chen, W.: Three Eurasian teleconnection patterns: spatial structures, temporal  
436 variability, and associated winter climate anomalies, *Clim. Dynam.*, 42, 2817–2839,  
437 <https://doi.org/10.1007/s00382-014-2163-z>, 2014.

438 Pu, X., Wang, T., Huang, X., Melas, D., Zanis, P., Papanastasiou, D., and Poupkou, A.: Enhanced surface ozone  
439 during the heat wave of 2013 in Yangtze River delta region, China, *Sci. Total Environ.*, 603, 807–816,  
440 <https://doi.org/10.1016/j.scitotenv.2017.03.056>, 2017.

441 Rayner, N., Parker, D. E., Horton, E., Folland, C., Alexander, L., Rowell, D., Kent, E., and Kaplan, A.: Global  
442 analyses of sea surface temperature, sea ice, and night marine air temperature since the late nineteenth century, *J.*

443 Geophys. Res.-Atmos., 108, 4407, <https://doi.org/10.1029/2002JD002670>, 2003.

444 Robinson, D. A., Dewey, K. F., and Heim, R. R.: Global snow cover monitoring: an update, *Bull. Amer. Meteor.*  
445 *Soc.*, 74, 1689–1696, [https://doi.org/10.1175/1520-0477\(1993\)074<1689:GSCMAU>2.0.CO;2](https://doi.org/10.1175/1520-0477(1993)074<1689:GSCMAU>2.0.CO;2), 1993.

446 Wallace, J. M., and Gutzler, D. S.: Teleconnections in the geopotential height field during the Northern  
447 Hemisphere winter, *Mon. Weather Rev.*, 109, 784–812, [https://doi.org/10.1175/1520-0493\(1981\)109<0784:TITGHF>2.0.CO;2](https://doi.org/10.1175/1520-0493(1981)109<0784:TITGHF>2.0.CO;2), 1981.

449 Wang, H. J., and He, S. P.: The North China/Northeastern Asia Severe Summer Drought in 2014, *J. Climate*, 28,  
450 6667–6681, <https://doi.org/10.1175/JCLI-D-15-0202.1>, 2015.

451 Wang, N., and Zhang, Y. C.: Evolution of Eurasian teleconnection pattern and its relationship to climate anomalies  
452 in China, *Clim. Dynam.*, 44, 1017–1028, <https://doi.org/10.1007/s00382-014-2171-z>, 2015.

453 Wei, J., Zhang, Q. Y., and Tao, S. Y.: Physical causes of the 1999 and 2000 summer severe drought in North China,  
454 *Chinese J. Atmos. Sci (in Chinese)*., 28, 125–137, <https://doi.org/10.1091/mbc.7.4.565>, 2004.

455 Wu, B., Zhang, R., Wang, B., and D'Arrigo, R.: On the association between spring Arctic sea ice concentration  
456 and Chinese summer rainfall, *Geophys. Res. Lett.*, 36, L09501, <https://doi.org/10.1029/2009GL037299>, 2009.

457 Yan, H., Duan, W., and Xiao, Z.: A study on relation between East Asian winter monsoon and climate change  
458 during raining season in China, *J. Trop. Meteor.*, 19, 367–376, <https://doi.org/10.3969/j.issn.1006-8775.2004.01.003>, 2003.

460 Yim, S. Y., Jhun, J. G., Lu, R., and Wang, B.: Two distinct patterns of spring Eurasian snow cover anomaly and  
461 their impacts on the East Asian summer monsoon, *J. Geophys. Res.- Atmos.*, 115, D22113,  
462 <https://doi.org/10.1029/2010JD013996>, 2010.

463 Yin, Z. C., Wang, H. J., Li, Y. Y., Ma, X. H., and Zhang, X. Y.: Links of climate variability among Arctic Sea ice,  
464 Eurasia teleconnection pattern and summer surface ozone pollution in North China, *Atmos. Chem. Phys.*, 19,  
465 3857–3871, <https://doi.org/10.5194/acp-19-3857-2019>, 2019.

466 Yin, Z. C., Yuan, D. M., Zhang, X. Y., Yang, Q., and Xia, S. W.: Different contributions of Arctic sea ice anomalies  
467 from different regions to North China summer ozone pollution, *Int. J. Climatol.*, 40, 559–571,  
468 <https://doi.org/10.1002/joc.6228>, 2020a.

469 Yin, Z. C., Li, Y. Y., and Cao, B. F.: Seasonal Prediction of Surface O<sub>3</sub>-related Meteorological Conditions in  
470 summer in North China, *Atmos. Res.*, 246, 105–110, <https://doi.org/10.1016/j.atmosres.2020.105110>, 2020b.

471 Zhang, R. N., Sun, C. H., and Li, W. J.: Relationship between the interannual variations of Arctic sea ice and  
472 summer Eurasian teleconnection and associated influence on summer precipitation over China, *Chinese J.*  
473 *Geophys (in Chinese)*., 61, 91–105, <https://doi.org/10.6038/cjg2018K0755>, 2018.

474 Zhang, R. N., Zhang, R. H., and Zuo, Z. Y.: Impact of Eurasian Spring Snow Decrement on East Asian Summer  
475 Precipitation, *J. Climate*, 30, 3421–3437, <https://doi.org/10.1175/JCLI-D-16-0214.1>, 2017.

476 Zheng, B., Tong, D., Li, M., Liu, F., Hong, C., Geng, G., Li, H., Li, X., Peng, L., Qi, J., Yan, L., Zhang, Y., Zhao,  
477 H., Zheng, Y., He, K., and Zhang, Q.: Trends in China's anthropogenic emissions since 2010 as the consequence  
478 of clean air actions, *Atmos. Chem. Phys.*, 18, 14095–14111, <https://doi.org/10.5194/acp-18-14095-2018>, 2018.

## 479 Table and Figure captions

480 **Figure 1.** (a) The normalized variation in JJA-mean OWI (black), EU index (blue), simulated MDA8 O<sub>3</sub> (red)  
481 from 1980 to 2018 and observed MDA8 O<sub>3</sub> (green) from 2014 to 2018 after detrending. (b) The 21-year sliding  
482 correlation coefficients between simulated MDA8 O<sub>3</sub> (red), OWI (black) and EU. The black dotted line (crosses)  
483 indicates (exceeded) the 95% confidence level. (c) Composite difference of the simulated MDA8 O<sub>3</sub> (unit:  $\mu\text{g m}^{-3}$ )  
484 in summer between the six highest and the six lowest EU index years from 1980 to 2018. The white dots (hatching)  
485 indicate that the difference was above the 95% (90%) confidence level (*t* test). The green box represents the  
486 location of North China. (d) Composite difference of the mass fluxes of summer ozone (unit:  $\text{tons d}^{-1}$ ) from the  
487 GEOS-Chem between the six highest and the six lowest EU years from 1980 to 2018. The left axis is the name of  
488 the physical-chemical processes: chemical reaction (Chem), transport (Trans), PBL mixing (Mix), convection  
489 (Conv) and their sums (Sum).

490 **Figure 2.** The correlation coefficients between the JJA-mean OWI and AM-mean snow cover (a) from 1980 to  
491 1998 and (b) from 1999 to 2018. The white dots (hatching) indicate that the correlation coefficients exceeded the  
492 95% (90%) confidence level (*t* test). The green box represents the key area used to calculate the SC<sub>sw</sub> index. The  
493 linear trend is removed.

494 **Figure 3.** The normalized variation in (a) OWI (black) and SC<sub>WS</sub> (red), (b) OWI (black) and SI<sub>GR</sub> (blue) from  
495 1980 to 2018 after detrending. The 21-year sliding correlation coefficients between (c) SC<sub>WS</sub> and OWI (red), EU  
496 (blue), (d) SI<sub>GR</sub> and OWI (red), EU (blue). The black dotted line (crosses) indicates (exceeded) the 95%  
497 confidence level. The linear trend is removed.

498 **Figure 4.** (a) The south edge of the 85% snow cover concentration during 1980–1993 (black) and during 2004–  
499 2018 (red). The gray (green) box represents the key area used to calculate the NHF<sub>WS</sub> (SC<sub>sw</sub>) index. The  
500 correlation coefficients between the SC<sub>WS</sub> × -1 and (b) surface net radiation flux (shortwave+longwave) and (c)  
501 surface net heat flux (latent+sensible) are displayed during 1980–1998 (shading) and 1999–2018 (contour). White  
502 dots (hatching) indicate that the correlation coefficients during P1 exceeding the 95% (90%) confidence level (*t*  
503 test). The gray (black) contours represent the correlation coefficients during P2 exceeding the 95% (90%)  
504 confidence level. The linear trend is removed.

505 **Figure 5.** The correlation coefficients between the SC<sub>WS</sub> × -1 (a, c), NHF<sub>WS</sub> (b, d) and surface air temperature  
506 (shading) and geopotential height at 500 hPa (contour) from 1980 to 1998 (a, b) and from 1999 to 2018 (c, d).  
507 The white dots (hatching) indicate that the correlation coefficients in shading exceeded the 95% (90%) confidence  
508 level (*t* test). The green boxes represent the anomalous cyclonic or anticyclonic centers in AM. The linear trend is  
509 removed.

510 **Figure 6.** (a) The normalized variation in the JJA OWI (black), JJA EU index (red) and AM NHF<sub>WS</sub> (blue) from  
511 1980 to 2018 after detrending. The numbers represent the correlation coefficients between the NHF<sub>WS</sub> and EU,  
512 OWI during 1980–1998 and 1999–2018, respectively. Two asterisks indicate that the correlation coefficients

513 exceeded the 95% confidence level. The correlation coefficients between  $SC_{WS} \times -1$  and JJA surface air  
514 temperature (shading) and geopotential height at 500 hPa (contour) from 1980 to 1998 (b) and from 1999 to 2018  
515 (c). The white dots (hatching) indicate that the correlation coefficients with surface air temperature exceeded the  
516 95% (90%) confidence level (t test). The green boxes represent the key areas used to calculate the EU index. The  
517 linear trend is removed.

518 **Figure 7.** The meteorological conditions associated with the  $SC_{WS} \times -1$ . (a, b) The correlation coefficients  
519 between  $SC_{WS} \times -1$  and precipitation (shading) and wind at 850 hPa (arrow); (c, d) surface incoming shortwave  
520 flux (shading), and the sum of low and medium cloud cover (contour) from 1980 to 1998 (a, c) and from 1999 to  
521 2018 (b, d). The white dots (hatching) indicate that the correlation coefficients represented with shading exceeded  
522 the 95% (90%) confidence level (t test). The gray (black) contours exceeded the 95% (90%) confidence level. The  
523 green boxes represent the location of North China. The linear trend is removed.

524 **Figure 8.** Composite difference of the summer MDA8  $O_3$  (unit:  $\mu g m^{-3}$ ) simulated by the GEOS-Chem model  
525 between the three lowest and the three highest  $SC_{WS}$  years (a) from 1980 to 1998 and (b) from 1999 to 2018. The  
526 white dots (hatching) indicate that the difference was above the 95% (90%) confidence level (t test). The green  
527 boxes represent the location of North China. The bar chart on the right is the composite difference of the summer  
528 mass fluxes of ozone (unit: tons d<sup>-1</sup>) during each periods. The left axis is the name of the physical-chemical  
529 processes: chemical reaction (Chem), transport (Trans), PBL mixing (Mix), convection (Conv) and their sums  
530 (Sum). The results were calculated within the planetary boundary layer.

531 **Figure 9.** (a) The variation in the JJA-mean observed OWI (black), the fitted OWI-1 (by the  $SC_{WS}$  and  $SI_{GR}$ , red),  
532 and the fitted OWI-2 (by the  $SC_{WS}$ ,  $SI_{GR}$  and  $SI_{CB}$ , blue) from 1980 to 2018 after detrending. (b) The 21-year  
533 sliding correlation coefficients between observed OWI and fitted OWI-1 (red), fitted OWI-2 (blue). The black  
534 dotted line (crosses) indicates (exceeded) the 95% confidence level.